ARTICLE

Microscopic Properties of Forces from Ice Solidification Interface Acting on Silica Surfaces Based on Molecular Dynamics Simulations

Received 00th January 20xx,
Accepted 00th January 20xx

DOI: 10.1039/x0xx00000x

Shota Uchida,*[a] Kunio Fujiwara [b] and Masahiko Shibahara [b]

The origin of the forces acting on a silica surface from an ice solidification interface was investigated to understand the solidification phenomenon and its impact on nanometer–scale structures using molecular dynamics simulations. The microscopic forces were determined by appropriately averaging the forces acting on the silica wall from the water molecules in time and space; the time evolutions of these microscopic forces during the solidification processes were investigated for three types of silica surfaces. The results indicate that the microscopic forces fluctuate more after the solidification interface makes contact with the wall surface. To visualize the changes in the microscopic forces and hydrogen bonds due to solidification, their differences compared to the liquid state were calculated. When the solidification interface is near the wall, the changes in these microscopic forces and hydrogen bonds due to solidification are correlated. This tendency is more significant for an amorphous wall and a wall with a structure than for a crystalline wall. The changes in the microscopic force depend on the water molecules that behave as acceptors when forming the hydrogen bonds with the wall and on the configuration of the silanol groups on the silica surfaces.

Introduction

On an ice surface or between ice and a solid wall, a layer commonly known as the quasi–liquid layer (QLL) forms in a pre–melt state. Several studies have investigated the QLLs of ice surfaces[1–3] and those between ice and substrates.[4] In particular, the QLL that occurs between ice interfaces and solid walls has been studied in various contexts, such as ice friction,[5,6] adsorption control,[7] and climate change.[8] Thus, several theoretical,[9–11] experimental, [12–23] and analytical[24–29] studies have examined the physical phenomena underlying the QLL and revealed that the QLL has a thickness of a few nanometers. In particular, a new cleaning method utilizing the solidification phenomenon has been proposed for the recent manufacturing of semiconductors miniaturized to a few nanometers.[30] Elucidating the solidification state of water molecules in the QLL at the substrate–ice interface and revealing the microscopic forces exerted by the solidification phenomena on the solid wall are important for understanding the pattern collapse of semiconductor structures and the removal mechanism of particles attached to wafers on the nanometer scale, which in turn, is necessary for the development of semiconductor cleaning processes.[31–36] Although the QLLs on silica walls used as semiconductor substrates have been investigated experimentally[37–40] and analytically,[41,42] the details of the microscopic forces acting on the solid wall from the solidification interface have not been clarified on the nanometer scale.

The forces of the solidification interface that act on spherical particles have been experimentally and theoretically investigated on the micrometer scale,[43] and water solidification in micrometer–scale channels has been experimentally observed.[44] However, it is unclear whether this micrometer–scale theory can be applied to microscopic forces from a solidification interface acting on nanoparticles. It is also unclear whether the space between the nanometer–scale channel solidifies.

Previous studies investigated the microscopic forces acting on smooth walls[45] and nanoparticle[46] via molecular dynamics (MD) simulations. In these studies, no hydrogen bonds explicitly formed between the water molecules and wall surfaces because smooth surfaces with Pt atoms were used in the MD simulations, which did not incorporate the atomic charges. However, a surface of the substrate, such as a Si wafer, contains natural oxide films in the hydroxylated amorphous state,[47,48] which also have nanometer scale roughness; for example, the pattern structures constructed on Si wafers. Several previous studies have investigated hydrogen bonds formed between silanol groups on silica surfaces and water molecules.[49–52] Their results imply that the force exerted by the water molecules on such walls is related to the hydrogen bonds formed between the water molecules and silanol groups.[53]

According to these studies, the forces due to solidification can be observed if they exceed the force exerted by the water

[a] SCREEN Holdings Co., Ltd., 322 Furukawa-cho, Hazukashi, Fushimi-ku, Kyoto, Kyoto 612-8486, Japan.
[b] Osaka University, 2-1 Yamadaoka, Suita, Osaka 565-0871, Japan.

†Electronic Supplementary Information (ESI) available: Parameters of simulation models, Density profiles near wall, Melting point confirmation, spectral properties of the microscopic forces, force probability distributions, hydrogen bonds between water molecules and silanol groups, and correlation between forces and layer thickness at silica–ice interface. See DOI: 10.1039/x0xx00000x

molecules in the liquid state on the wall surface. Moreover, any change in the former would be difficult to observe because of the dominance of random forces at the nanometer scale. These results suggest that temporal and spatial averaging of the forces is necessary to eliminate the fluctuations of the forces due to random forces and to observe the forces due to solidification. However, to our knowledge, no studies have employed temporal and spatial averaging to observe the changes in the forces due to the solidification phenomenon. Moreover, the effects of solidification interfaces on amorphous silica walls with nanometer scale roughness, such as semiconductor structures, are unclear. Thus, it remains unclear whether the water molecules in the nanometer regions between these structures crystallize.

The purpose of this study is to elucidate the forces acting on a solid wall from a nearby solidification interface using non–equilibrium MD simulations. We use a silica wall as a solid wall model and simulate the solidification of water molecules. Simulations are conducted for a coexistence system of water and ice on hydroxylated flat crystalline and amorphous silica surfaces and an amorphous silica wall with a structure before and after contact with the solidification interface. To observe the changes in the forces due to the solidification phenomenon, we define forces averaged appropriately in time and space as the microscopic forces. Focusing on the hydrogen bonds between the water molecules and silanol groups on the silica wall surface, we investigate the time evolution of the microscopic forces, the number of hydrogen bonds, and the duration for which the hydrogen bonds are maintained. The changes due to solidification are estimated for each variable based on the differences from their mean values in the liquid state, to clearly visualize the effects of the solidification phenomena. Next, we evaluate the correlation coefficients between the changes in the hydrogen bonds and the forces due to solidification, and analyse the effects of these correlations on the conditions of the silica walls.

Computational method

Silica surface model

In this study, three types of silica wall models were prepared: crystalline and amorphous planes and a wall with a structure on the amorphous plane. The crystalline and amorphous planes were constructed using a procedure described in Ref. 42 to obtain equivalent silica surfaces. The size of the crystalline and amorphous planes was $L_x \times L_y \times L_z$ = 2.20 × 2.33 × 2.20 nm^3 and were composed of 300 Si atoms and 600 O atoms, respectively. The structure of the crystalline silica was the α–quartz, and the orientation of the surface was (100). The amorphous plane was obtained by annealing crystalline silica using the following procedure. First, the temperature of the calculation system was raised from 1 K to 5000 K for 0.2 ns to melt the crystal structure, and then the system was maintained at 5000 K for 0.8 ns to equilibrate. Subsequently, the system was quenched at 240 K to obtain an amorphous structure. The Nosé–Hoover thermostat was used for temperature controls. Next, a vacuum region of 2.0 nm was set along the *z*–direction, and the upper boundary condition in the *z*–direction was changed from a periodic boundary condition to a mirror boundary condition. This change in the boundary condition introduced an unnatural surface structure along the *z*–direction. The second annealing step was performed to optimize the surface structure by annealing the calculation system to 800 K. The procedure used to prepare the wall surface with a structure was similar to that used for the amorphous silica wall surface. A silica crystal structure consisting of 600 Si atoms and 1200 oxygen atoms was established within the simulation system shown in Fig. 1, which had a size of $L_x \times L_y \times L_z$ = 4.40 × 2.33 × 2.20 nm^3. Annealing at 5000 K was simulated to create an amorphous wall. Then, the SiO_2 atoms were removed so that the structure height, width, and spacing values were each 2.0 nm. Annealing at 800 K was then simulated for the calculation system to relax the atomic configuration. Finally, silanol groups were attached to the dangling bonds on three types of silica surfaces.

The simulations to build the silica walls were performed using the Tersoff potential prepared for the SiO system.[54] Either H or OH was attached to dangling bonds on the wall surfaces. The Tersoff potentials previously prepared for the SiOH system[55,56] were used in calculations to calculate the silica wall surface containing H atoms.

The three types of silica wall surfaces investigated in this study are denoted as “flat crystalline”, “flat amorphous” and “structured amorphous”, respectively. Figure 1 shows details of each region in the “structured amorphous” model. The following discussion of the “structured amorphous” refers to the $Wall_{top}$ region in Fig. 1, which is the top region of the structure.

For the “flat crystalline” and “flat amorphous”, the surface position perpendicular to the wall was determined using the peak position of the density profile of the O atoms for the silanol groups,[42] and the position of the surfaces in the *z*–direction was defined as the origin. For the “structured amorphous”, the position of the origin in the *z*–direction was defined as the bottom surface, i.e., that at the base of the structure shown in Fig. 1.

The densities of silanol groups on each wall surface were 7.20, 4.69, and 4.85 /nm^2 for the “flat crystalline”, “flat amorphous”, and “structured amorphous” surfaces, respectively, consistent with the results of previous studies.[48,57,58]

Water model

The ice–water coexistence system established for the “flat crystalline” and “flat amorphous” had 1224 water molecules (3672 atoms) and dimensions of $L_x \times L_y \times L_z$ = 2.20 × 2.33 × 7.80 nm^3. The water–ice coexistence system used for the “structured amorphous” was obtained using a similar procedure, with a calculation system consisting of 2448 water molecules and dimensions of $L_x \times L_y \times L_z$ = 4.40 × 2.33 × 7.80 nm^3. In order to obtain the ice–water coexistence system, crystallized ice blocks were prepared with the corresponding system size for each wall surface. Each simulation system has periodic boundary conditions in all directions. First, to create the liquid region, the simulation boxes were divided into two areas in the *z*–direction.

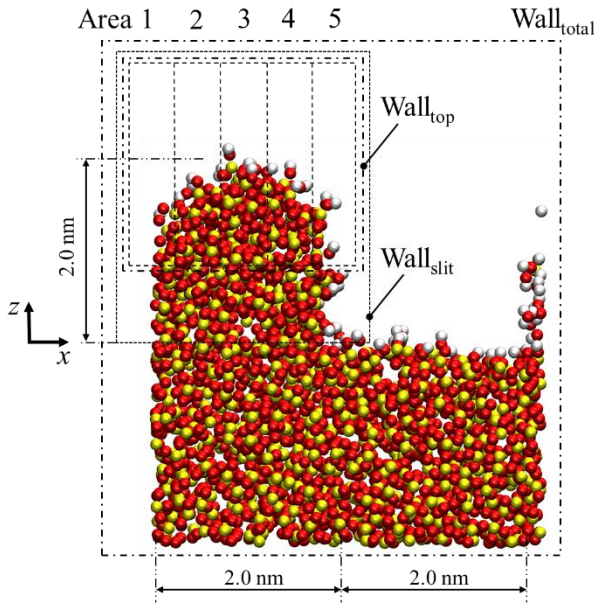

Fig.1 Side view of the "structured amorphous" model and the region details.

The temperature of each region was controlled at 300 K on the lower side (wall side) and 1 K on the upper side using the velocity scaling method for 1 ns. Subsequently, the temperature of the entire system was controlled at 200 K for 1 ns using the Nosé–Hoover thermostat. The ice region has a hexagonal ice structure and the plane orientation of the ice–water interface is {1120}.

The TIP4P/2005 model[59] was used for the water molecules, and calculations were performed with a 2 fs time interval.

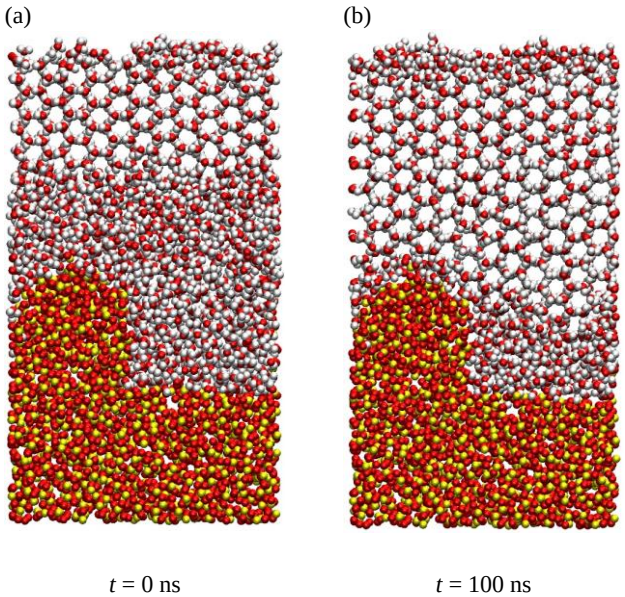

Fig. 2 Snapshots of the solidification process at t = 0 and 100 ns for the "structured amorphous".

Simulation conditions

The ice–water coexistence systems were placed on wall surfaces established using the procedures described above. The calculation system dimensions were set to $L_x \times L_y \times L_z$ = 2.20 × 2.33 × 12.0 nm^3 on the walls of the "flat crystalline" and "flat amorphous", and $L_x \times L_y \times L_z$ = 4.40 × 2.33 × 12.0 nm^3 on the wall of the "structured amorphous". A vacuum region with a thickness of approximately 2.0 nm in the z–direction was set above the ice region as the initial condition for each calculation system. In these three calculation systems, a periodic boundary condition was applied in the x and y directions, and a mirror boundary condition was applied in the z–direction.

The interaction between the water molecules and the silica surface was calculated using the 12–6 Lennard–Jones potential and Coulomb potential,

$$\phi_{ij}(r_{ij}) = 4\varepsilon_{ij}\left\{\left(\frac{\sigma_{ij}}{r_{ij}}\right)^{12} - \left(\frac{\sigma_{ij}}{r_{ij}}\right)^{6}\right\} + \frac{q_i q_j}{4\pi\varepsilon_0 r_{ij}} \qquad (1)$$

where i and j are the numbers of atoms and r_{ij} is the distance between the two atoms. The Lorenz–Berthelot mixing rule was used to obtain the LJ parameters of σ_{ij} and ε_{ij} between the different atoms. q_i and q_j are the partial charges of the atoms. The LJ parameters and charges for the silica walls were from previous studies[60] and the consistency of the setting of the interaction were confirmed using the density profiles of the water molecules perpendicular to the silica surface[61] and the thickness of the QLL at silica–ice interface[42]. The details of the parameters for water molecules and silica wall, and density profiles of water molecules are provided in the Electronic Supplementary Information.

The RESPA method [63] was used to apply different time–step widths to the calculations for the water molecules and silica walls, i.e., 2 and 0.1 fs, respectively. The large–scale atomic/molecular massively parallel simulator (LAMMPS)[64] was used in the calculations.

Simulation procedure

The simulation of the solidification processes of water molecules on the three types of silica walls was simulated using the following procedure. After increasing the temperature of the entire system from 1 K to the cooling temperature in 1 ns, the calculation was performed without temperature control for 1 ns to relax the system. Subsequently, the temperature of the water molecules in the cooling area (the region above the ice phase: 7.0 nm < z < 8.0 nm), referred to as the cooling temperature in this study, was controlled using the velocity scaling method. During the entire calculation period, the wall temperature was maintained at the same temperature as that of the cooling area using the Langevin method.

In the calculations for the "flat crystalline" and "flat amorphous", the initial atomic configurations were modified from those described in Ref. 42, to facilitate comparison with the case of the "structured amorphous" surface.

Snapshots of the solidification processes on the "structured amorphous" are shown in Fig. 2.

Result and discussion

Solidification process

First, the melting point of each calculation system was investigated to simulate the solidification process. In MD simulations of solidification processes, the potential energy of the water molecules decreases with crystallization.[65,66] In this study, the melting point of the calculation system was determined from the change in the total energy (sum of potential and kinetic energies). The melting points of the simulation systems were determined to be 238, 241, and 242 K for the "flat crystalline", "flat amorphous", and "structured amorphous", respectively. Details are provided in the Electronic Supplementary Information. A solidification interface grows when the target temperature of the calculation system is lower than the melting point. In this study, the difference between the melting point and cooling temperature was defined as the degree of supercooling, with $T_{\text{degree of supercooling}} = T_{\text{melting point}} - T_{\text{cooling temperature}}$.

The degrees of supercooling of the "flat crystalline", "flat amorphous", and "structured amorphous" were 3, 3, and 9 K, respectively. Figure 3 shows the time evolution of the solidification interface on each surface. The position of the solidification interface was equivalent to the *z*–directional coordinates of the ice crystal closest to the wall surface. Because the surface of the walls was defined as the origin in the *z*–direction, *d* (Fig. 3) indicates the distance between the wall surface and solidification interface. The ice crystals were distinguished by the lifetimes of the hydrogen bonds between~~contained in~~ water molecules, and the hydrogen bonds of each water molecule were determined from the associated coordinate positions using geometrical criteria; (a) a distance of less than 0.25 nm between donor H atom and acceptor O atom; (b) a distance of less than 0.35 nm between donor O atom and acceptor O atom; (c) an angle of less than 30° between the direction of the donor O–acceptor O vector and the OH–bond vector of the donor.[67,68]

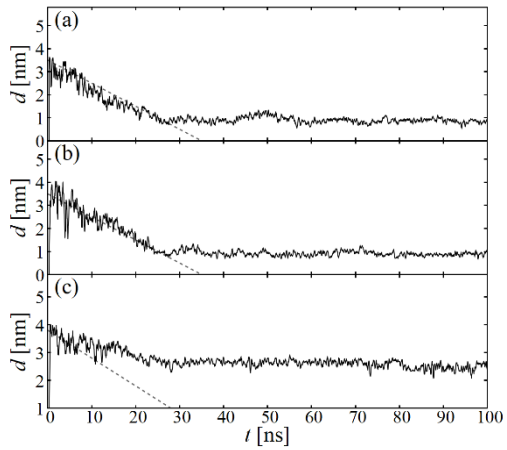

Fig. 3 Time evolutions of the ice-crystal minimum *z* position for (a) flat crystalline, (b) flat amorphous, and (c) structured amorphous surfaces.

The growth behaviors of the solidification interfaces shown in Fig. 3 indicate that the growth rates of ice crystals on the "flat crystalline" and "flat amorphous" were equivalent at 10 cm/s from the slope of the dashed line, and that the solidification interface reached the wall at approximately t = 20 ns. For the "structured amorphous", the growth rate of the solidification interface immediately after the start of the calculation ($0 < t <$ 10 ns) was equivalent to that for the "flat crystalline" and "flat amorphous". The ice–crystal growth rates obtained in this study are in good agreement with those obtained for bulk ice using the TIP4P/2005 water model.[69] For the "structured amorphous", the growth rate of the solidification interface decelerated after 10 ns. This is because the growth at $0 < t < 10$ ns occurred in the bulk liquid region above the structure, whereas in later periods, the growth occurred in the region near the structure and between the solidification interface and the structure. Although the degree of supercooling for the "structured amorphous" (9 K) exceeded those for the "flat crystalline" and "flat amorphous" (3 K), similar growth rates of the solidification interface were obtained in the bulk liquid region. Thus, the solidification phenomena near the three types of silica walls could be calculated under approximately equivalent cooling conditions. After the solidification interface made contact with the wall surface, a liquid layer of approximately 1 nm thickness was maintained between the silica surface and solidification interface in the "flat crystalline" and "flat amorphous". This liquid layer was the QLL discussed in the introduction, and the QLL thicknesses obtained in this study are consistent with the findings of previous experimental[37,39] and analytical studies.[42]

For the "structured amorphous", the solidification interface fluctuated at approximately d = 2.5 nm, as shown in Fig.3 (c). Because d represents the distance from the bottom surface of the structure to the solidification interface, and as the height of the structure was approximately 2 nm, this result indicates that the water molecules in the region between the structures were in a liquid state, and that permanent ice crystallization such as that typically observed in a bulk region did not occur at the bottom region of the structures. We confirmed that the solidification interface fluctuated near the top area of the structure, and that the fluctuations in the solidification interface shown in Fig. 2 (b) continued during the calculation.

Microscopic forces from solidification interface

The force acting on a given wall can be divided into the force from the water molecules F_{water} and the force from the atoms constituting the wall F_{wall}, and is expressed as $F_{\text{total}} = F_{\text{water}} + F_{\text{wall}}$. F_{water} was the sum of the forces exerted by the water molecules on all atoms constituting the silica wall and calculated by using the following equation.

$$F_{\text{water}} = \sum_{i}^{n_{\text{water}}} \sum_{j}^{n_{\text{silica}}} F_{ij} \qquad (2)$$

In this study, the area size of the "flat crystalline" ,"flat amorphous", and inspection area Wall_{top} used in "structured amorphous" are set to be equivalent and converted to the unit~~s~~ of pressure. On the other hand, previous studies[70,71] have reported that the local pressure near a nanometer slit differs

from the pressure in a plane. In order to focus on the discussion of force, we define force in this study as the sum of forces acting between atoms in the calculation system. Figure 4 shows the time evolution of F_{water} during the solidification process on each silica wall. The *x*, *y*, and *z* symbols in Fig. 4 represent the force components in each direction. The forces indicated by the gray and black lines are the time averaged values for 0.01 and 0.25 ns, respectively. Note that time averaging for 0.25 ns removes the THz–order frequency forces generated by the water molecule rotation[72]. Details of the force spectrum information used to determine the averaging time are provided in the Electronic Supplementary Information. The forces shown in Figs. 4 (a)–(c) represent the sums of the forces acting on the entire wall surface for the "flat crystalline", "flat amorphous", and "structured amorphous", respectively, where the latter surface corresponds to the $Wall_{top}$ region shown in Fig. 1. The 0.25 ns averaged forces represented by the black lines in Fig. 4, were defined as the microscopic forces.

As shown in Fig. 3, the solidification interface made contact with the wall at approximately t = 20 ns for each silica surface. However, it was difficult to confirm significant differences in the time evolutions of the microscopic forces after solidification shown in Fig. 4.

To investigate the differences in the microscopic forces after solidification, the force time evolutions shown in Fig. 4 were divided into time regions of t = 0–20, 20–40, 40–60, 60–80, and 80–100 ns, respectively. Figure 5 shows the probability distribution functions of the microscopic forces for t = 0–20 ns (liquid water) and 80–100 ns (ice). From Fig. 5, the distributions of the forces acting on the "flat crystalline" and "flat amorphous" were close to normal. However, in the "structured amorphous", the probability distribution function was not normal and had multiple peaks, which implies that the forces from the water molecules acting on the wall surface were biased and that forces of a specific intensity were exerted on the structure.

When the forces before and after the solidification interface made contact with the wall surface are compared for the "flat crystalline", it is apparent that the probability distribution function did not change significantly. However, for the "flat amorphous" and "structured amorphous", the force distribution ranges broadened after the solidification interface made contact with the wall, as is apparent from the *x*–axis of Fig. 5 (b) and the *x*– and *z*–directions of Fig.5 (c). These results indicate that a larger force acts on a wall surface when a solidification interface is nearby. However, we confirmed that such changes after solidification were not observed for the probability distributions of the 0.01 ns averaged forces. Details are provided in the Electronic Supplementary Information. The results of the probability distributions of the 0.25 ns averaged forces indicate that it is possible to qualitatively visualize the changes in microscopic forces appropriately averaged in time and space owing to the solidification phenomena.

To clarify these force changes, we focused on the hydrogen bonds between the water molecules and silanol groups on the silica wall.

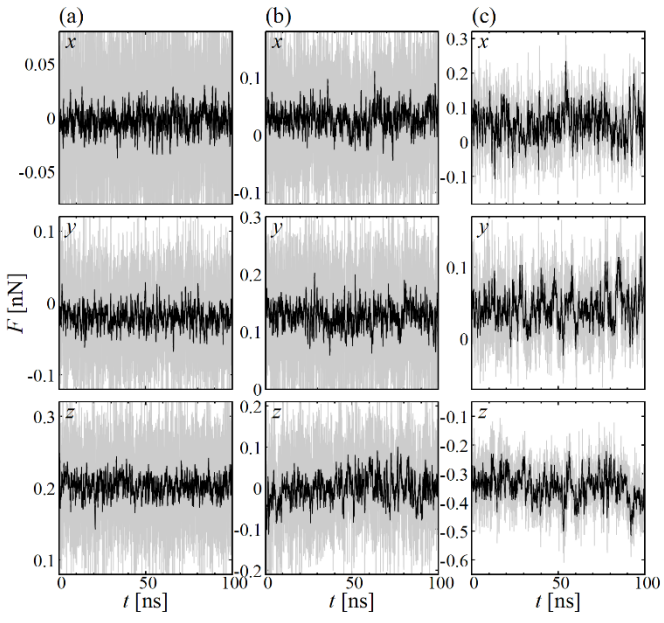

Fig. 4 Time evolutions of forces from water molecules acting on silica walls for (a) flat crystalline, (b) flat amorphous and (c) structured amorphous surfaces. The gray and black lines show the time–averaged values at 0.01 and 0.25 ns, respectively.

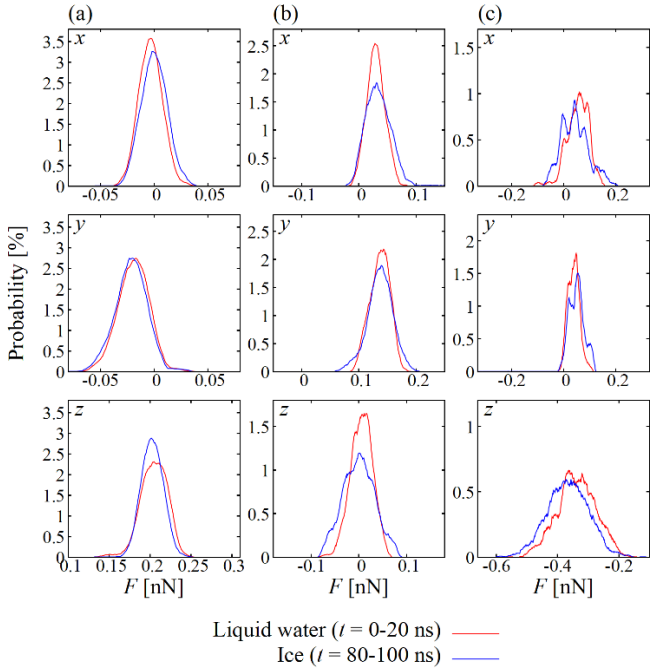

Fig. 5 Probability distributions of microscopic forces from water molecules acting on the silica surfaces shown in Fig. 4: (a) flat crystalline, (b) flat amorphous, and (c) structured amorphous surfaces. The forces used to calculate the distribution functions were averaged at 0.25 ns.

Hydrogen bonds between water molecules and silanol groups

In this study, two types of hydrogen bonds between water molecules and silanol groups were assumed, i.e., cases in which the water molecule behaved as an acceptor of the hydrogen bond or a donor of the hydrogen bond to the silanol group. These conditions were labeled "a" and "d" respectively, as shown in Fig. 6 (a) and (b). The hydrogen bonds were identified based on the associated coordinate position using geometrical criteria.[62] Figure 6 presents an example involving a geminal silanol group based on a calculation considering the hydrogen bonds between isolated silanol groups and water molecules. In the figure, the black dotted line between the water molecule and silanol group represents a hydrogen bond. A water molecule can form four hydrogen bonds, with two donors and two acceptors of hydrogen bonds. Thus, a water molecule that forms a hydrogen bond with a silanol group also has 1–3 hydrogen bonds with other water molecules. In this study, we distinguished the hydrogen bonds using a_0–a_3 and d_0–d_3 labels, where the subscript numbers refer to the number of the hydrogen bonds between the water molecule having the hydrogen bond with the silanol group and another water molecule, as shown in Fig. 6 (c) – (h). Further, a_{total} and d_{total} indicate all hydrogen bonds of types a_0–a_3 and d_0–d_3, respectively. The number of water molecules having hydrogen bonds as donors and acceptors for silanol groups was calculated and defined as n, and the average time for which the hydrogen bonds between the water molecules and silanol groups were maintained was defined as δt.

The time evolutions of n and δt on each silica wall are shown in Fig. 7. The numbers of donors and acceptors were similar in the "flat amorphous" shown in Fig. 7 (b), whereas the number of acceptors exceeded the number of donors for the "flat crystalline" shown in Fig. 7 (a). This is because there was a greater number of silanol groups on the surface in the "flat crystalline" than "flat amorphous". In contrast, for the "structured amorphous" shown in Fig. 7 (c), the number of donors was larger because this surface had a convex shape and the arrangement interval of silanol groups was wider. As shown in Fig. 7, the sum of the donors and acceptors on each wall surface was approximately 17, which was equivalent on each wall. The calculation systems were comparable in terms of size, and the number of the hydrogen bonds between the water molecules and silanol groups was expected to depend on the areas of the silica wall surfaces.

The δt results are shown in the second row of Fig. 7. A smaller δt was obtained for the "flat crystalline" than for the "flat amorphous" shown in Figs. 7 (a) and (b). This outcome indicates that the hydrogen bond formation was repeated over a short period in the "flat crystalline". For each silica wall, there was no significant difference between the δt values of the donors and acceptors. However, the fluctuations in δt increased after t = 20 ns for the "flat amorphous" and "structured amorphous". The fluctuations in n and δt for a_2–, a_3–, d_2–, and d_3–type hydrogen bonds were all larger after t = 20 ns, suggesting a trend similar to that shown in Fig. 7. Details of the n and δt values for each type of hydrogen bond are provided in the Electronic Supplementary Information.

This finding on the time evolution of the hydrogen bonds is consistent with the microscopic force trend shown in Fig. 4 and attributed to the effect of the contact of the solidification interface with the silica wall surface.

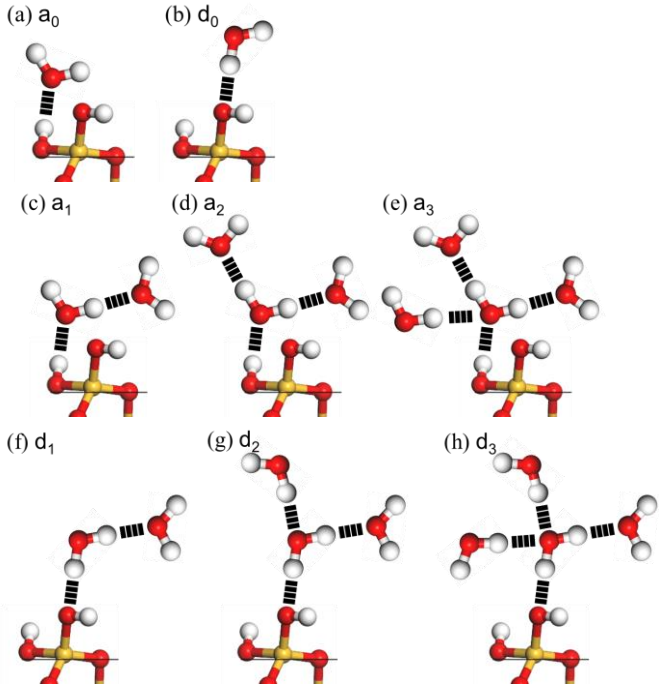

Fig. 6 Schemes showing hydrogen bonds formed between water molecules and silanol groups where a water molecule is a hydrogen–bond (a) acceptor or (b) donor. Schemes showing multiple hydrogen bonds between other water molecules and a water molecule with silanol groups: water molecules are hydrogen bond (c)–(e) acceptors and (f)–(h) donors.

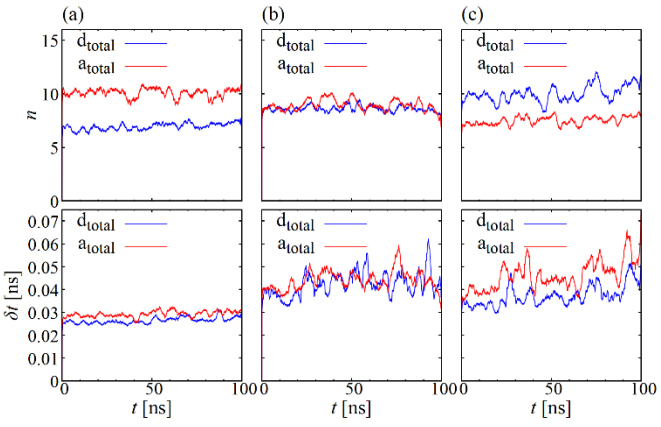

Fig. 7 Time evolutions of the numbers of water molecules forming hydrogen bonds with silanol groups (n, upper) and the durations for which the hydrogen bonds were maintained (δt, lower) for the (a) flat crystalline, (b) flat amorphous, and (c) structured amorphous surfaces. The blue and red lines indicate donor (d_{total}) and acceptor (a_{total}) values for each variable.

Changes in forces and hydrogen bonds due to solidification

In the following section, we discuss a method for quantitatively investigating the changes in the forces and hydrogen bonds owing to the contact of the solidification interface with the wall surface. To evaluate the changes due to solidification in the microscopic forces from the water molecules acting on the silica wall, *F*, the following equations were used. Note that values for the *n* and δt variables were calculated using a similar procedure.

$$\bar{F}_{\mathrm{liquid}} = \frac{1}{t_{\mathrm{liquid}}}\int_0^{t_{\mathrm{liquid}}} F(t)dt \tag{3}$$

$$\sigma_{\mathrm{liquid}} = \sqrt{\frac{1}{t_{\mathrm{liquid}}}\int_0^{t_{\mathrm{liquid}}} \left(F(t)-\bar{F}_{\mathrm{liquid}}\right)^2 dt} \tag{4}$$

$$F_{\mathrm{ice}}(t) = \begin{cases} F(t)-\bar{F}_{\mathrm{liquid}}, & \left|F(t)-\bar{F}_{\mathrm{liquid}}\right| > 3\sigma_{\mathrm{liquid}} \\ 0, & \left|F(t)-\bar{F}_{\mathrm{liquid}}\right| \le 3\sigma_{\mathrm{liquid}} \end{cases} \tag{5}$$

The mean value (in this case, $\bar{F}_{\mathrm{liquid}}$) and deviation ($\sigma_{\mathrm{liquid}}$) of each variable were determined for the period when the water molecules in the vicinity of the wall were in the liquid state ($0 \le t \le t_{\mathrm{liquid}}$). The difference from the mean value in the liquid state ($F_{\mathrm{ice}}(t)$ in this case) was calculated for each variable when the changes exceeded the values in the liquid state ($\pm 3\sigma_{\mathrm{liquid}}$) for $t_{\mathrm{liquid}} \le t \le 100$ ns. In this study, F_{ice} was defined as the force calculated from *F* using Equations (3)–(5) to clearly visualize the changes due to solidification, and the same definition was applied to n_{ice} and δt_{ice}. The time at which the solidification interface made contact with the wall was $t_{\mathrm{liquid}} = 20$ ns. The time evolutions calculated for each variable are shown in Fig. 8.

As is apparent from the time evolutions of each variable shown in Fig. 8, only minor changes occurred in response to the contact of the solidification interface with the "flat crystalline". By contrast, significant changes due to solidification were apparent for the "flat amorphous" and "structured amorphous".

To evaluate the details of the results in Fig.8, the maximum values of $n_{\mathrm{ice}}(t)$, $\delta t_{\mathrm{ice}}(t)$ and $F_{\mathrm{ice}}(t)$ during the solidification process are presented in Tables 1–3, respectively. The mean value and deviation of each variable in the liquid state (0 < *t* < 20 ns) were calculated from the results of Figs. 4 and 7.

Here, n_{ice} changed in the range of 1.08–2.41 after the solidification interface made contact with the wall; this is approximately 10 % of the sum of the donor and acceptor hydrogen bond counts of 17 for the simulation area, according to Fig. 7. Moreover, the $\delta t_{\mathrm{liquid}}$ values on the "flat crystalline" were 0.025 and 0.028 ns for the hydrogen bond donor and acceptor water molecules, as detailed in Tables 1 and 2, respectively. Following contact of the solidification interface with the "flat crystalline", δt_{ice} was 0.0058 ns, indicating an increase of approximately 20 % in δt owing to solidification. However, for the "flat amorphous" and "structured amorphous", δt_{ice} increased by 50–100 % of the pre–solidification value.

Similar to the trend in the hydrogen bond changes for the "flat crystalline", the changes in F_{ice} were small. For the "flat amorphous" and "structured amorphous", the intensities of the

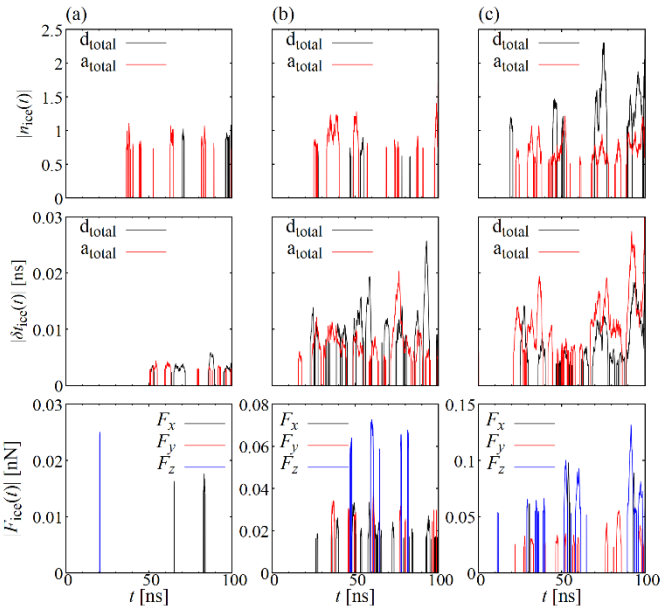

Fig. 8 Time evolution of $n_{i\,\mathrm{ice}}(t)$, $t_{i\,\mathrm{ice}}(t)$ and $F_{\mathrm{ice}}(t)$; (a) flat crystalline, (b) flat amorphous and (c) structured amorphous surfaces.

changes in F_{ice} after solidification depended on the direction. For example, for the "structured amorphous", the mean value of F_{liquid} in the *x*–direction was 0.052 nN, whereas the change in the force due to solidification, i.e., F_{ice} was 0.098 nN. This result implies that the force from the solidification interface was approximately 0.15 nN, and that the maximum value of F_{ice} increased by approximately three times following contact of the solidification interface with the wall surface.

These results indicate that the changes in the forces and hydrogen bonds due to solidification were larger on amorphous surfaces than on crystalline surfaces.

Correlations between forces and hydrogen bonds

To investigate the correlations between the forces from the water molecules acting on the wall surface and the hydrogen bonds between the water molecules and silanol groups, we defined the following function *I*, which returns 1 if F_{ice}, n_{ice} and δt_{ice} are non–zero values:

$$I(F_{\mathrm{ice}}(t)) = \begin{cases} 1, & F_{\mathrm{ice}}(t) \ne 0 \\ 0, & F_{\mathrm{ice}}(t) = 0 \end{cases} \tag{6}$$

$$I(n_{\mathrm{ice}}(t)) = \begin{cases} 1, & n_{\mathrm{ice}}(t) \ne 0 \\ 0, & n_{\mathrm{ice}}(t) = 0 \end{cases} \tag{7}$$

$$I(\delta t_{\mathrm{ice}}(t)) = \begin{cases} 1, & \delta t_{\mathrm{ice}}(t) \ne 0 \\ 0, & \delta t_{\mathrm{ice}}(t) = 0 \end{cases} \tag{8}$$

The function *G*, which returns 1 when F_{ice}, n_{ice} and δt_{ice} are simultaneously non–zero, is described by the following equations:

$$G(F_{\mathrm{ice}}, n_{\mathrm{ice}}) = I\left(F_{\mathrm{ice}}(t)\right) I\left(n_{\mathrm{ice}}(t)\right) \tag{9}$$

$$G(F_{\mathrm{ice}}, \delta t_{\mathrm{ice}}) = I\left(F_{\mathrm{ice}}(t)\right) I\left(\delta t_{\mathrm{ice}}(t)\right) \tag{10}$$

The following correlation coefficients were calculated to evaluate the correlation between the hydrogen bonds, n_{ice}, and δt_{ice} with respect to F_{ice}:

$$\sigma_{IG} = \frac{1}{t}\int_0^t (I(t)-\bar{I})(G(t)-\bar{G})dt \quad (11)$$

$$\sigma_I = \sqrt{\frac{1}{t}\int_0^t (I(t)-\bar{I})^2 dt} \quad (12)$$

$$\sigma_G = \sqrt{\frac{1}{t}\int_0^t (G(t)-\bar{G})^2 dt} \quad (13)$$

$$r(I,G) = \frac{\sigma_{IG}}{\sigma_I \sigma_G} \quad (14)$$

The correlation coefficients between F_{ice} and n_{ice}, and between F_{ice} and t_{ice}, can be expressed as $r(I(F_{\mathrm{ice}}), G(F_{\mathrm{ice}}, n_{\mathrm{ice}}))$ and $r(I(F_{\mathrm{ice}}), G(F_{\mathrm{ice}}, \delta t_{\mathrm{ice}}))$, respectively. An $r(I,G)$ value of 1 indicates that the changes due to contact of the solidification interface with the wall surface occurred simultaneously for the two associated variables. Further, $\bar{I}$ and $\bar{G}$ represent the mean values calculated using Equation (3).

The $r(I(F_{\mathrm{ice}}), G(F_{\mathrm{ice}}, n_{\mathrm{ice}}))$ and $r(I(F_{\mathrm{ice}}), G(F_{\mathrm{ice}}, \delta t_{\mathrm{ice}}))$ results for each silica wall type are shown in Fig. 9. For the "structured amorphous", results are shown for each area defined in Fig. 1. In Fig. 9 (a), the $r(I(F_{\mathrm{ice}}), G(F_{\mathrm{ice}}, n_{\mathrm{ice}}))$ result for the "flat crystalline" is large because F_{ice} remained almost unchanged in this simulation; thus, Equation (9) became zero, and consequently, Equation (14) became small. For the "flat amorphous" and "structured amorphous", $r(I(F_{\mathrm{ice}}), G(F_{\mathrm{ice}}, n_{\mathrm{ice}}))$ exceeded 0.5 for the acceptor of water molecules, indicating a correlation. For the water molecules acting as donors of hydrogen bonds, the relationship between F_{ice} and n_{ice} was less correlated than that for the water molecules acting as acceptors. However, in some regions, such as Area 3 in Fig. 1 for the "structured amorphous", $r(I(F_{\mathrm{ice}}), G(F_{\mathrm{ice}}, n_{\mathrm{ice}}))$ exceeded 0.5, indicating a correlation between F_{ice} and n_{ice}.

In Fig. 9 (b), the $r(I(F_{\mathrm{ice}}), G(F_{\mathrm{ice}}, \delta t_{\mathrm{ice}}))$ results indicate a stronger correlation than that between F_{ice} and n_{ice} shown in Fig. 9 (a). In particular, $r(I(F_{\mathrm{ice}}), G(F_{\mathrm{ice}}, \delta t_{\mathrm{ice}}))$ exceeded 0.7 for the "flat amorphous" and for several areas of the "structured amorphous", indicating a strong correlation between F_{ice} and δt_{ice}. A comparison of the $r(I(F_{\mathrm{ice}}), G(F_{\mathrm{ice}}, \delta t_{\mathrm{ice}}))$ results obtained for the donors and acceptors of hydrogen bonds confirmed that the acceptors tended to be more correlated with F_{ice} than the donors.

Table 1 Values of n and δt for water molecules forming hydrogen bonds with silanol groups as donors (d_{total}).

	n_{liquid}	σ_{liquid}	max($n_{ice}(t)$)	δt_{liquid}	σ_{liquid}	max($\delta t_{ice}(t)$)
Flat crystalline	6.65	0.85	1.08	0.025	0.002	0.0058
Flat amorphous	8.57	0.63	1.07	0.036	0.009	0.026
Structured amorphous	9.73	0.98	2.41	0.033	0.003	0.003

Table 2. Values of n and δt for water molecules forming hydrogen bonds with silanol groups as acceptors (a_{total}).

	n_{liquid}	σ_{liquid}	max($n_{ice}(t)$)	δt_{liquid}	σ_{liquid}	max($\delta t_{ice}(t)$)
Flat crystalline	10.0	0.70	1.11	0.028	0.003	0.0043
Flat amorphous	8.84	0.73	1.96	0.039	0.004	0.020
Structured amorphous	7.12	0.49	1.22	0.038	0.006	0.038

Table 3. Forces from water molecules acting on walls.

	$F_{x\,liquid}$	$\sigma_{Fx\,liquid}$	max($\lvert F_{x\,ice}(t)\rvert$)
Flat crystalline	-0.0033	0.014	0.018
Flat amorphous	0.029	0.016	0.034
Structured amorphous	0.052	0.061	0.098

	$F_{y\,liquid}$	$\sigma_{Fy\,liquid}$	max($\lvert F_{y\,ice}(t)\rvert$)
Flat crystalline	-0.019	0.021	0
Flat amorphous	0.13	0.024	0.040
Structured amorphous	0.041	0.023	0.056

	$F_{z\,liquid}$	$\sigma_{Fz\,liquid}$	max($\lvert F_{z\,ice}(t)\rvert$)
Flat crystalline	0.21	0.022	0.025
Flat amorphous	-0.24	0.056	0.073
Structured amorphous	-0.33	0.051	0.13

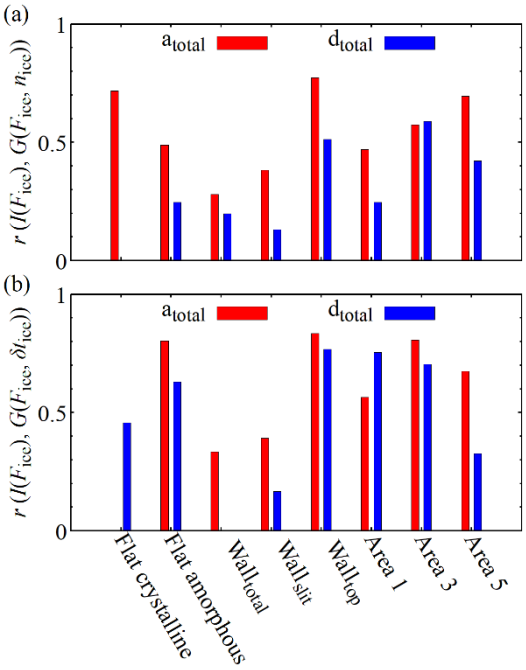

Fig. 9 Correlations between forces from water molecules acting on silica walls and hydrogen bonds for correlation coefficients of (a) F_{ice} and n_{ice} and (b) F_{ice} and δt_{ice}.

From Figs. 9 (a) and (b), the correlation coefficients were lower than approximately 0.3 for the $Wall_{total}$ and $Wall_{slit}$ regions of the "structured amorphous". This is because the water molecules in the inspection areas remained in a liquid state with no ice crystallization. However, in Areas 1, 3, and 5, where the water molecules form ice crystals in the vicinity of the silica surfaces, $r(I(F_{ice}), G(F_{ice}, n_{ice}))$ and $r(I(F_{ice}), G(F_{ice}, \delta t_{ice}))$ exceeded 0.5. These results indicate that the changes in the forces from the water molecules acting on the wall surface due to the solidification phenomena were caused by the hydrogen bonds between the water molecules and silanol groups.

Although the correlation between the force and thickness of the liquid layer at the silica–ice interface *d* shown in Fig. 3 was also investigated using a similar procedure as that used to obtain the results in Fig. 9, we could not confirm a clear correlation. Details are provided in the Electronic Supplementary Information.

Finally, we investigated the point at which the water molecules forming hydrogen bonds with silanol groups as acceptors correlated more strongly with F_{ice} than those acting as donors. Figure 10 show the configurations of the water molecules forming hydrogen bonds with silanol groups on the three types of silica wall considered in this study. Figures 10 (a) and (b) depict the results before (t = 0–15 ns) and after (t = 85–100 ns) the solidification interface made contact with the wall surfaces, respectively. In Fig. 10, the water molecules that formed hydrogen bonds with silanol groups as acceptors (red dots) are located closest to the silanol groups, whereas those that formed hydrogen bonds with silanol groups as donors (blue dots) are located outside of the acceptors. The orange dots depict the water molecules at the tip of the solidification interface. These water molecules were distributed farther from the wall surfaces than the acceptor and donor water molecules. From Fig. 10, the water molecules forming the hydrogen bonds with the silanol groups as acceptors were closest to the wall surface for all silica wall types. This result suggests strong correlation between the water molecules acting as acceptors and the forces acting on the wall surfaces from the water molecules.

As depicted in Fig. 9, better correlations existed between the hydrogen bonds and the forces of the water molecules as donors for the "flat amorphous" and "structured amorphous" than that for the "flat crystalline". For the latter, water molecules that behaved as acceptors of hydrogen bonds were located in the vicinity of the periodically configured silanol groups, whereas those that behaved as donors for hydrogen bonds were located farther from the wall surface. Therefore, the effect of the water molecules that behaved as donors on the wall surface was weak, and the correlation coefficients were, correspondingly, smaller.

For the "flat amorphous" and "structured amorphous" with randomly configured silanol groups, it is thought that the correlations between the forces and the donor water molecules increased because the donor water molecules were closer to the wall surface at locations where the silanol groups were widely located. For the $Wall_{top}$ region of the "structured amorphous", which had a convex surface shape, the silanol groups were more widely distributed than in the "flat amorphous" and water molecules as donors were existed closer to the wall surfaces. This result was substantiated by the correlation coefficients between the donor water molecules, and the forces at the "structured amorphous" were larger than those at the other walls, as shown in Fig. 9. This trend implies that the increased contribution of the donor water molecules is responsible for the larger force change due to solidification on the amorphous walls.

These results clarify that the change in the force acting on the wall due to contact with the solidification interface was caused by the changes in the hydrogen bonds between silanol groups on the silica surface and water molecules. In particular, the contact of the solidification interface with the wall surface significantly changed the duration of the hydrogen bonds between the water molecules and silanol groups. These results also confirm that the changes in the forces acting on the wall due to solidification were more strongly influenced by the water molecules forming hydrogen bonds with the silanol groups as acceptors than those acting as donors. As acceptor water molecules were abundant closest to the wall surface, the changes due to solidification affected the forces acting on both crystalline and amorphous walls. In contrast, the effect of the changes in donor water molecules due to solidification was more significant on amorphous walls than on crystalline walls, which was due to the random configuration of the silanol groups. On amorphous surfaces, the changes due to solidification of the donor water molecules in addition to the acceptor water molecules affect the changes in forces. This induces larger changes in forces on an amorphous surface compared to those on a crystalline surface.

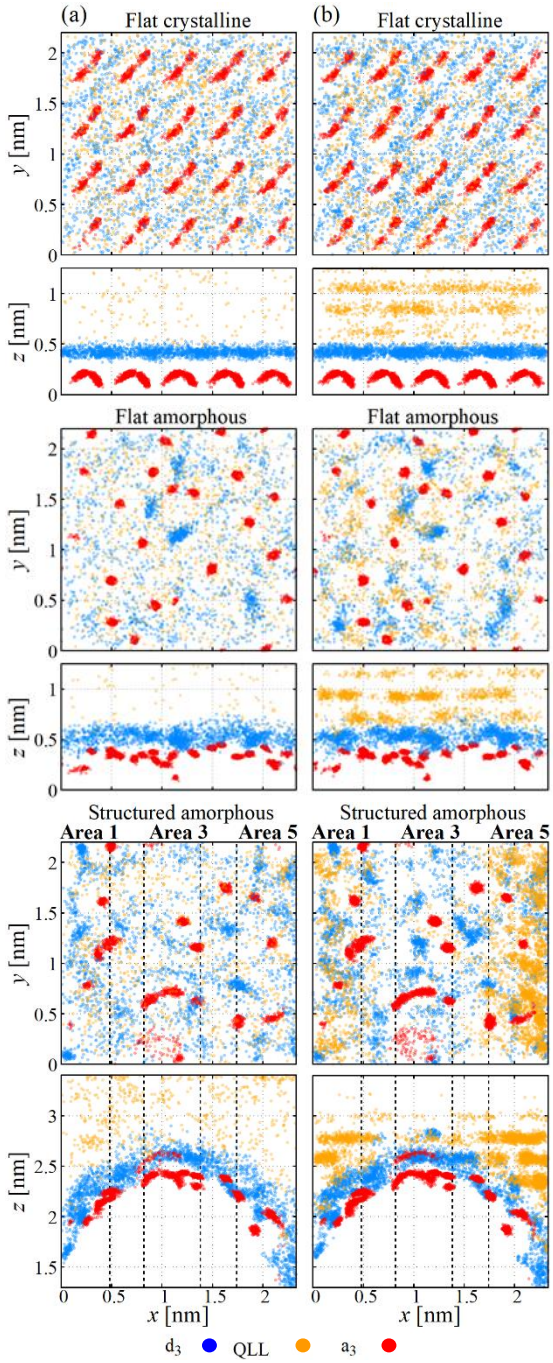

Fig. 10 Configurations of water molecules with acceptors and donors of hydrogen bonds and ice–crystal minimum position (QLL) on the "flat crystalline"', "flat amorphous", and "structured amorphous" surfaces at (a) t = 0–15 ns and (b) t = 85–100 ns.

Conclusion

MD simulations of solidification processes were conducted on "flat crystalline", "flat amorphous", and "structured amorphous" silica wall surfaces for an approaching solidification interface. In the calculation systems used in this study, the microscopic forces from water molecules acting on the wall surfaces were obtained by averaging appropriately in time and space. The time evolution of the microscopic force showed a qualitative tendency for the fluctuation to increase with the approach of the solidification interface to the wall surface.

To investigate the force changes as the solidification interface made contact with each wall surface, we focused on the hydrogen bonds formed between water molecules and silanol groups. The changes in the number of hydrogen bonds and the duration over which the hydrogen bonds fluctuated more after the solidification interface made contact with the wall surface. We used the mean values and deviations in the liquid state to visualize the changes in the forces and hydrogen bonds due to the solidification phenomena. Consequently, we quantitatively evaluated the change in each variable due to solidification and found that the change in the number of hydrogen bonds after solidification was approximately 10 % of that before solidification, whereas the hydrogen bond maintenance duration after solidification was approximately twice that before solidification. In addition, the force acting on the wall surface from the water molecules was approximately thrice that before solidification. These changes in the forces and hydrogen bonds due to solidification were more significant when the silica walls had a rough surface, indicating a random configuration of silanol groups and structures on the surfaces.

The change in the number of hydrogen bonds, the hydrogen bonds maintenance duration, and the forces acting on the wall surface from the water molecules owing to solidification were evaluated using correlation coefficients. The results indicate that the force change is strongly related to the change in the hydrogen bond maintenance duration. It was clarified that the force change due to solidification is influenced by the water molecules that form the hydrogen bonds with silanol groups as acceptors on a crystalline wall. On an amorphous wall, changes in the donor water molecules due to solidification affect the wall surface in addition to the effect of the acceptor water molecules, and this behaviour depend on the configurations of the silanol groups on the silica surfaces.

In conclusion, this study clarified that the solidification phenomenon changes the microscopic forces acting on a wall surface and identified the cause of these force changes through hydrogen bonds. We believe that the results may improve understanding of solidification phenomena near wall surfaces on the nanoscale level. Although we have investigated the correlation between microscopic forces and hydrogen bonds, we did not directly determine the relationship between forces and the behaviour of ice interfaces. This relationship will be investigated in future studies.

Conflicts of interest

There are no conflicts to declare.

Acknowledgements

No specific grants from funding agencies in the public, commercial, or not-for-profit sectors were received for this study.

Notes and references

1 C. L. Hosler, D. C. Jensen and L. Goldshlak, *J. Atmos. Sci.*, 1957, **14**, 415–420.
2 C. R. Hosler, *Mon. Weather Rev.*, 1961, **89**, 319–339.
3 H. H. G. Jellinek and F. Flajsman, *J. Polym. Sci. Part A-1 Polym. Chem.*, 1969, **7**, 1153–1168.
4 Y. Li and G. A. Somorjai, *J. Phys. Chem. C*, 2007, **111**, 9631–9637.
5 R. Rosenberg, *Phys. Today*, 2005, **58**, 50–55.
6 J. H. Lever, E. Asenath-Smith, S. Taylor and A. P. Lines, *Front. Mech. Eng.*, 2021, **7**, 1–19.
7 K. A. Emelyanenko, A. M. Emelyanenko and L. B. Boinovich, *Coatings*, 2020, **10**, 648.
8 T. Bartels-Rausch, *Nature*, 2013, **494**, 27–29.
9 I. E. Dzyaloshinskii, E. M. Lifshitz and L. P. Pitaevskii, *Adv. Phys.*, 1961, **10**, 165–209.
10 L. A. Wilen, J. S. Wettlaufer, M. Elbaum and M. Schick, *Phys. Rev. B*, 1995, **52**, 12426–12433.
11 L. B. Boinovich and A. M. Emelyanenko, *Adv. Colloid Interface Sci.*, 2002, **96**, 37–58.
12 T. Bartels-Rausch, H. W. Jacobi, T. F. Kahan, J. L. Thomas, E. S. Thomson, J. P. D. Abbatt, M. Ammann, J. R. Blackford, H. Bluhm, C. Boxe, F. Domine, M. M. Frey, I. Gladich, M. I. Guzmán, D. Heger, Th. Huthwelker, P. Klán, W. F. Kuhs, M. H. Kuo, S. Maus, S. G. Moussa, V. F. McNeill, J. T. Newberg, J. B. C. Pettersson, M. Roeselová and J. R. Sodeau, *Atmos. Chem. Phys.*, 2014, **14**, 1587–1633.
13 Y. Nagata, T. Hasegawa, E. H. G. Backus, K. Usui, S. Yoshimune, T. Ohto and M. Bonn, *Phys. Chem. Chem. Phys.*, 2015, **17**, 23559–23564.
14 Y. Furukawa and I. Ishikawa, *J. Cryst. Growth*, 1993, **128**, 1137–1142.
15 K. Morishige and K. Nobuoka, *J. Chem. Phys.*, 1997, **107**, 6965–6969.
16 K. Morishige, *J. Phys. Chem. C*, 2018, **122**, 5013–5019.
17 H. Li, M. Bier, J. Mars, H. Weiss, A. C. Dippel, O. Gutowski, V. Honkimäki and M. Mezger, *Phys. Chem. Chem. Phys.*, 2019, **21**, 3734–3741.
18 A. Endo, T. Yamamoto, Y. Inagi, K. Iwakabe and T. Ohmori, *J. Phys. Chem. C*, 2008, **112**, 9034–9039.
19 H. J. Butt, A. Döppenschmidt, G. Hüttl, E. Müller and O. I. Vinogradova, *J. Chem. Phys.*, 2000, **113**, 1194–1203.
20 B. Pittenger, S. C. Fain, Jr., M. J. Cochran, J. M. K. Donev, B. E. Robertson, A. Szuchmacher and R. M. Overney, *Phys. Rev. B - Condens. Matter Mater. Phys.*, 2001, **63**, 1–15.
21 G. Algara-Siller, O. Lehtinen, F. C. Wang, R. R. Nair, U. Kaiser, H. A. Wu, A. K. Geim and I. V. Grigorieva, *Nature*, 2015, **519**, 443–445.
22 J. M. Yuk, J. Park, P. Ercius, K. Kim, D. J. Hellebusch, M. F. Crommie, J. Y. Lee, A. Zettl and A. P. Alivisatos, *Science*, 2012, **335**, 61–64.
23 G. Sazaki, H. Asakawa, K. Nagashima, S. Nakatsubo and Y. Furukawa, *Cryst. Growth Des.*, 2013, **13**, 1761–1766.
24 J. A. Hayward and A. D. J. Haymet, *J. Chem. Phys.*, 2001, **114**, 3713–3726.
25 H. Nada and Y. Furukawa, *J. Cryst. Growth*, 2005, **283**, 242–256.
26 T. Kling, F. Kling and D. Donadio, *J. Phys. Chem. C*, 2018, **122**, 24780–24787.
27 X. X. Zhang, Y. J. Lü and M. Chen, *Mol. Phys.*, 2013, **111**, 3808–3814.
28 E. B. Moore, E. de la Llave, K. Welke, D. A. Scherlis and V. Molinero, *Phys. Chem. Chem. Phys.*, 2010, **12**, 4124–4134.
29 A. Nouri-Khorasani, K. Malek and M. Eikerling, *Electrocatalysis*, 2014, **5**, 167–176.
30 K. Miya, N. Fujiwara, M. Kato and A. Izumi, *ECS Trans.*, 2011, **41**, 215–220.
31 M. N. Chong, B. Jin, C. W. K. Chow and C. Saint, *Water Res.*, 2010, **44**, 2997–3027.
32 J. An, H. Lee, H. Kim and H. Jeong, *Jpn. J. Appl. Phys.*, 2012, **51**, 026501.
33 K. Fujiwara and M. Shibahara, *Nano. Micro. Therm. Eng.,* 2013*,* **17***,* 1–9.
34 T. Tanaka, M. Morigami and N. Atoda, *Jpn. J. Appl. Phys.*, 1993, **32**, 6059–6064.
35 Y. Sasaki, T. Yamazaki and Y. Kimura, *ACS Appl. Nano Mater.*, 2022, **5**, 9495–9502.
36 S. Uchida, K. Fujiwara and M. Shibahara, *Nanoscale Microscale Thermophys. Eng.*, 2020, **24**, 53–65.
37 S. Engemann, H. Reichert, H. Dosch, J. Bilgram, V. Honkimäki and A. Snigirev, *Phys. Rev. Lett.*, 2004, **92**, 205701.
38 A. Anderson and W. R. Ashurst, *Langmuir*, 2009, **25**, 11549–11554.
39 J. F. D. Liljeblad, I. Furó and E. C. Tyrode, *Phys. Chem. Chem. Phys.*, 2017, **19**, 305–317.
40 Y. R. Huang, K. H. Liu, C. Y. Mou and C. K. Sun, *Appl. Phys. Lett.*, **107**, 081607.
41 J. Yang, S. Meng, L. F. Xu and E. G. Wang, *Phys. Rev. Lett.*, 2004, **92**, 1–4.
42 S. Uchida, K. Fujiwara and M. Shibahara, *J. Phys. Chem. B*, 2021, **125**, 9601–9609.
43 D. R. Uhlmann, B. Chalmers and K. A. Jackson, *J. Appl. Phys.*, 1964, **35**, 2986–2993.
44 J. Friedrich, C. Reimann, T. Jauss, A. Cröll and T. Sorgenfrei, *J. Cryst. Growth*, 2016, **447**, 18–26.
45 K. Fujiwara, S. Sasaki and M. Shibahara, *Therm. Sci. Eng.*, 2016, **25**, 9–16.
46 T. Miyamotoa, K. Fujiwara and M. Shibahara, *7th Asian Symp. Comput. Heat Transf. Fluid Flow*, 2019, 6–7.
47 M. Morita, T. Ohmi, E. Hasegawa, M. Kawakami and M. Ohwada, *J. Appl. Phys.*, 1990, **68**, 1272–1281.
48 L. T. Zhuravlev, *Colloids Surfaces A Physicochem. Eng. Asp.*, 2000, **173**, 1–38.
49 D. Argyris, D. R. Cole and A. Striolo, *J. Phys. Chem. C*, 2009, **113**, 19591–19600.
50 A. Phan, T. A. Ho, D. R. Cole and A. Striolo, *J. Phys. Chem. C*, 2012, **116**, 15962–15973.
51 S. Dewan, V. Carnevale, A. Bankura, A. Eftekhari-Bafrooei, G. Fiorin, M. L. Klein and E. Borguet, *Langmuir*, 2014, **30**, 8056–8065.
52 S. Pezzotti, D. R. Galimberti and M. P. Gaigeot, *Phys. Chem. Chem. Phys.*, 2019, **21**, 22188–22202.
53 Y. Huang, X. Zhang, Z. Ma, Y. Zhou, W. Zheng, J. Zhou and C. Q. Sun, *Coord. Chem. Rev.*, 2015, **285**, 109–165.
54 S. Munetoh, T. Motooka, K. Moriguchi and A. Shintani, *Comput. Mater. Sci.*, 2007, **39**, 334–339.
55 F. De Brito Mota, J. F. Justo and A. Fazzio, *J. Appl. Phys.*, 1999, **86**, 1843–1847.
56 J. A. Martinez-Gonzalez, N. J. English and A. A. Gowen, *AIP Adv.*, 2017, **7**, 115105.
57 E. Papirer, *Surfactant Science Series*, 2000, Dekker.
58 A. Rimola, D. Costa, M. Sodupe, J. F. Lambert and P. Ugliengo, *Chem. Rev.*, 2013, **113**, 4216–4313.
59 J. L. F. Abascal and C. Vega, *J. Chem. Phys.*, 2005, **123**, 234505.
60 T. J. Hou, L. L. Zhu and X. J. Xu, *J. Phys. Chem. B*, 2000, **104**, 9356–9364.
61 A. A. Milischuk and B. M. Ladanyi, *J. Chem. Phys.*, 2011, **135**, 174709.

62 F. Musso, S. Casassa, M. Corno and P. Ugliengo, *Struct. Chem.*, 2017, **28**, 1009–1015.
63 M. Tuckerman, B. J. Berne and G. J. Martyna, *J. Chem. Phys.*, 1992, **97**, 1990–2001.
64 S. Plimpton, *J. Comput. Phys.*, 1995, **117**, 1–19.
65 R. García Fernández, J. L. F. Abascal and C. Vega, *J. Chem. Phys.*, 2006, **124**, 144506.
66 K. Koga, H. Tanaka and X. C. Zeng, *Nature*, 2000, **408**, 564–567.
67 A. Luzar and D. Chandler, *Nature*, 1996, **379**, 55–57.
68 M. Matsumoto, S. Saito and I. Ohmine, *Nature*, 2002, **416**, 409–413.
69 R. A. Nistor, T. E. Markland and B. J. Berne, *J. Phys. Chem. B*, 2014, **118**, 752–760.
70 K. Fujiwara and M. Shibahara, *J. Chem. Phys.*, 2014, **141**, 034707.
71 K. Fujiwara and M. Shibahara, *J. Chem. Phys.*, 2015, **142**, 094702.
72 J. J. Max and C. Chapados, *J. Chem. Phys.*, 2009, **131**, 184505.